Applied Catalysis B: Environmental 242 (2019) 19–30

Contents lists available at ScienceDirect

Applied Catalysis B: Environmental

journal homepage: www.elsevier.com/locate/apcatb

Directional electron delivery and enhanced reactants activation enable efficient photocatalytic air purification on amorphous carbon nitride co-functionalized with O/La

Peng Chen[a], Hong Wang[a], Hongjing Liu[b], Zilin Ni[a], Jieyuan Li[c], Ying Zhou[d], Fan Dong[a,d,*]

[a] Chongqing Key Laboratory of Catalysis and New Environmental Materials, College of Environment and Resources, Chongqing Technology and Business University, Chongqing 400067, China
[b] College of Resource and Environmental Science, Chongqing University, Chongqing 400045, China
[c] College of Architecture and Environment, Sichuan University, Chengdu 610065, China
[d] The Center of New Energy Materials and Technology, School of Materials Science and Engineering, Southwest Petroleum University, Chengdu 610500, China

ARTICLE INFO

Keywords:
Amorphous carbon nitride
Photocatalysis mechanism
NO removal
Electron delivery pathway
Reactants activation

ABSTRACT

Graphitic carbon nitride (g-C_3N_4) is an intriguing and rising visible light photocatalyst. However, g-C_3N_4 still suffers from random charge carriers transfer in planes and low efficiency in reactants activation, which leads to unsatisfactory photocatalytic efficiency. Herein, these formidable challenges are addressed via a new strategy of O/La co-functionalization in amorphous carbon nitride (C N-O La), leading to the formation of electronic channels for directional electron delivery in the interlayers, the generation of localized electrons for enhanced reactants activation and thus highly boosted photocatalytic performance for NO removal. With a closely combined experimental and theoretical approach, we have revealed that the breakage of in-plane hydrogen bonds between strands of polymeric melon units with CO_3^{2-} could promote the amorphization of g-C_3N_4 and increase the visible light absorption ability. A directional electron delivery pathway (L2 → La → L1→ O) is proposed based on results of charge difference distribution and experimental observation. The electron localization could directly activate the O_2 and NO molecules and dramatically promote the production of activated species (e.g. O_2^- and OH radicals) and thus enhancing the photocatalytic efficiency. With the optimized electronic structure, the photocatalytic NO removal ratio of C N-O La is significantly increased from 35.8% of pristine g-C_3N_4 to 50.4% and it is stable for recycled runs. The *in situ* FT-IR spectra, in combination with ESR spectra and DFT calculations, unravel the conversion pathway of photocatalytic NO oxidation on C N-O La where some important reaction intermediates are discovered. This work could provide a fascinating modification strategy for carbon nitride and new insights into mechanistic understanding of 2D layered photocatalysts.

1. Introduction

Semiconductor photocatalysis has been widely studied because of its promising applications in addressing the issues of clean energy and environmental remediation [1–4]. Basic processes involved in semiconductor photocatalytic reactions include: (1) the generation of electrons/holes pairs under light irradiation; (2) the separation and migration of photogenerated electrons and holes; (3) the photocatalytic redox reaction with charge carriers [5,6]. According to above processes, the promotion of separation and transportation of charge carriers should be fully considered to enhance the photocatalytic activity. Also, the reactants activation associated with surface reaction plays a crucial role in improving the photocatalytic efficiency.

Lately, two-dimensional (2D) layered materials have received broad interests because of their tunable electronic structure for photocatalytic reaction [7]. Especially, the graphitic carbon nitride (g-C_3N_4, labeled as CN), a typical 2D semiconductor with layered structure, has demonstrated adjustable electronic structure and glorious physicochemical properties [8–10]. Unfortunately, the photocatalytic performance of the pristine CN is unsatisfactory due to the insufficient light-absorbance, the randomly charge carriers transfer in planes, and low efficiency in charge separation and reactants activation [11–13]. Thus, various strategies including surface functionalization (metal deposition, construction of heterojunctions), inner architecture optimization

* Corresponding author at: Chongqing Key Laboratory of Catalysis and New Environmental Materials, College of Environment and Resources, Chongqing Technology and Business University, Chongqing 400067, China.
E-mail address: dfctbu@126.com (F. Dong).

https://doi.org/10.1016/j.apcatb.2018.09.078
Received 20 August 2018; Received in revised form 17 September 2018; Accepted 25 September 2018
Available online 27 September 2018
0926-3373/ © 2018 Elsevier B.V. All rights reserved.

(elemental doping and microstructure design), cocatalyst modification and construction of core-shell structure have been developed for enhancing the photocatalytic performance of CN by efficiently separating photogenerated charges [14–16].

Elemental doping is one of the most effective approaches to enhance the photocatalytic performance of CN via the band structure and charge carriers regulation. Specifically, alkali metal doping in CN has been reveal to bridge the adjacent layers and thus drive carrier transfer between neighboring layers, which could further promote charge separation efficiency [17–19]. Recently, our group demonstrated that K, Rb and Cs could bridge the adjacent layers of CN to build electron delivery channels and motivate electrons to transfer between neighboring CN layers [20,21]. Furthermore, bioriented channels between adjacent layers were constructed via the intercalation of K and NO_3^- species to reduce energy barrier and steer the charge flow toward opposite direction [22].

Lanthanide ions possess the unique properties of forming ligand/coordination with other light elements in the interaction of these functional groups with the orbital of lanthanides [23–25]. Thus, incorporation of lanthanide ions into carbon nitride could modify the electronic structure of carbon nitride and thus potentially improve optical and charge transfer properties. Additionally, the amount of La as rare earth in China is rich and unique. Thus, La element was chosen to be introduced into the interlayer of carbon nitride in the aim to enhance the charge transfer and the photocatalytic activity via the interaction of La and functional group of carbon nitride. To the best of knowledge, the O/La co-functionalized amorphous carbon nitride to eliminate NO_x has never been reported.

In this work, O/La co-functionalized amorphous carbon nitride (C N-O La) was fabricated via the co-pyrolysis of urea with the $La_2(CO_3)_3$. When the g-C_3N_4 is made amorphous, the charge transfer efficiency should be increased as the charge could transfer in a short-rang manner in instead of long-rang manner. With a combined experimental and theoretical approach, we discovered that the O/La co-functionalization enables the formation of electron delivery channels in layered CN and the generation of electron localization. Here, electron localization refers to the electronic states in C N-O La could go from extended states to localized states and the electrons are mainly localized around O atom on the surface of CN owing to its strong electronegativity [26]. The amorphization of CN originated from the breakage of in-plane hydrogen bonds between strands of polymeric melon units by the CO_3^{2-}. The introduction of O and La would induce the formation of directional electron transportation channels (L2 → La → L1→ O), which could reduce the energy barriers for electron transfer between adjacent layers and further facilitate the reactants activation. Specifically, the boosted separation and transportation efficiency of charge carriers would provide numerous electrons to activate O_2 molecules and dramatically induce the production of activated species (e.g. O_2- and OH radicals) to participate in the photocatalytic redox reaction. Simultaneously, localized electrons could be also generated by the O/La co-functionalization, which could activate reactants (e.g. NO) to form intermediates (e.g. NO^+) and vastly enhance the photocatalytic efficiency. The *in situ* FT-IR spectra, in combination with ESR spectra and DFT calculations, revealed the conversion pathway of photocatalytic NO oxidation on CN and CN–OLa. This work sheds new light on the enhancement of photocatalytic performance of pristine CN via introducing La into interlayer and bonding O to the surface of CN. The new strategy could be potentially extended to other layered 2D photocatalysts.

2. Experimental section

2.1. Catalyst preparation

All chemicals employed in this study were of analytical grade and were used without further treatment. The C N-O La samples were synthesized via co-pyrolysis of urea and $La_2(CO_3)_3$. Firstly, 20 g of urea and a known amount of $La_2(CO_3)_3$ (1, 5, 10, 25, 50 wt.%, calculated via the following equation: α wt.% = $La_2(CO_3)_3$ / [($La_2(CO_3)_3$ + CN] were added in an alumina crucible (50 mL) and stirred by glass rod. Then the solid composite precursor placed in a semiclosed alumina crucible with a cover and calcined at 550 °C for 2 h with a heating rate of 15 °C/min in static air. After the thermal treatment, the crucible was cooled to room temperature and the samples with different weight ratios (1, 5, 10, 25, 50 wt. %) were collected and labeled as C N-O La-1, C N-O La-5, C N-O La-10, C N-O La-25 and C N-O La-50, respectively.

2.2. Characterization

The crystal phases of the samples were analyzed by X-ray diffraction (XRD) with CuKα radiation (Model D/max RA, Rigaku Co., Japan). X-ray photoelectron spectroscopy (XPS) with Al*Kα* X-ray radiation (hν = 1486.6 eV) operated at 150 W (Thermo ESCALAB 250, USA) was used to investigate the surface properties. Scanning electron microscopy (SEM, Model JSM-6490, Japan) and transmission electron microscopy (TEM, JEM-2010, Japan) were used to characterize the morphology and structure. Nitrogen adsorption-desorption isotherms were obtained on a nitrogen adsorption apparatus (ASAP 2020, USA) with all samples degassed at 300 °C for 4 h before measurements. Electron spin resonance (ESR) of radicals spin-trapped by 5,5-dimethyl-1-pyrroline N-O xide (DMPO) was recorded on a JES FA200 spectrometer. Samples for ESR measurement were prepared by mixing the samples in 50 mM DMPO solution tanks (aqueous dispersion for DMPO-OH and methanol dispersion for DMPO-O_2^-) and irradiated with visible light. Electron paramagnetic resonance (EPR) measurements were carried out on a Bruker ESP 500 spectrometer. Steady and time-resolved fluorescence emission spectra were recorded at room temperature with a fluorescence spectrophotometer (Edinburgh Instruments, FLSP-920). Photoluminescence (PL) studies (F-7000, HITACHI, Japan) and UV–vis diffuse reflectance spectra (UV–vis DRS) were obtained for the dry-pressed disk samples using a scanning UV–vis spectrophotometer (UV-2450, Shimadzu, Japan) equipped with an integrating sphere assembly to investigate the optical properties of the samples. The X-ray absorption fine structure (XAFS) to further study the structure of samples.

2.3. DFT calculations

Density functional theory (DFT) calculations were conducted using the Vienna *ab initio* simulation package (VASP5.4) [27,28], applying a generalized gradient correlation functional [29]. A plane-wave basis set with cutoff energy 450 eV was employed within the framework of the projector-augmented wave method [30,31]. The Gaussian smearing width was set to 0.2 eV. The Brillouin zone was sampled with a 3 × 3 × 1 Monkhorst Pack grid. All atoms were converged to 0.01 eV/Å. *Ab initio* molecular dynamics (AIMD) was carried out to verify the breakage of in-plane hydrogen bonds between strands of polymeric melon units by CO_3^{2-} and released CO_2 but left O. A 2 × 2 × 3 supercell of bulk g-C_3N_4 (CN) was first relaxed, and the calculated N−C bond length was consistent with the published values [32]. Then the model of La atoms and CO_3^{2-} species placed in the plane or interlayer of CN was also calculated for comparison via the total energy (E_{tot}) of the adsorption complex (Fig. S1).

2.4. In situ DRIFTS study of visible light photocatalytic NO oxidation process

The *in situ* DRIFTS measurements were conducted using a TENSOR II FT-IR spectrometer (Bruker) equipped with an in situ diffuse reflectance cell (Harrick) and a high-temperature reaction chamber (HVC), as shown in Scheme 1. The reaction chamber was equipped with three gas ports and two coolant ports. High-purity He, high-purity O_2, and 100 ppm of NO (in He) mixtures could be fed into the reaction system, and a three-way ball valve was used to switch between the

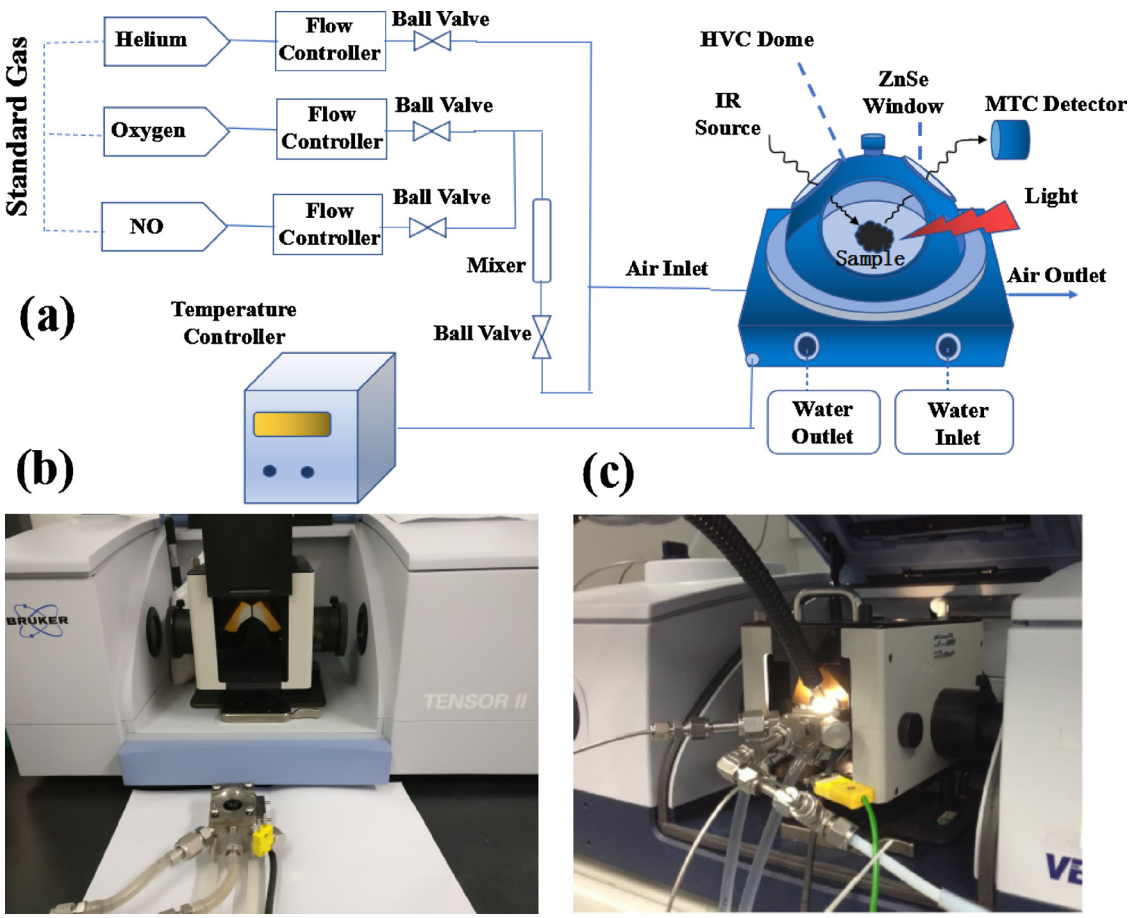

Scheme 1. The *in situ* FT-IR reaction cell: schematic diagram (a), Tensor II FT-IR spectrometer (Bruker) and loading parts (b) and *in situ* FT-IR measurement under working condition (c).

target gas (NO) and the purge gas (He). The total gas flow rate was 100 mL/min, and the concentration of NO was adjusted to 50 ppm by dilution with O_2. The chamber was enclosed with a dome having three windows, two for IR light entrance and detection, and one for illuminating the photocatalyst. The observation window was made of UV quartz and the other two windows were made of ZnSe. A Xe lamp (MVL-210, Japan) was used as the irradiation light source. In this work, prepared samples were pretreated for 20 min at 300 °C before measurements. In addition, the temperature was kept at 60 °C in whole measurement.

2.5. Evaluation of photocatalytic activity

Gas phase catalytic performance is evaluated through removal ratio of low concentration of NO with ppb revels (500 ppb) in the continuous flow reactor (rectangular reactor, 30 × 15 × 10 cm). The low concentration of NO with water vapor was prepared using standard air and NO standard gases with an original concentration of 100 ppm. Respectively taken 0.1 g samples in two small beakers that each one was added 20 ml distilled water, and transferred to two glass dishes (12.0 cm in diameter) after ultrasonic dispersion for 5 min, and dried at 60 °C to take catalytic activity tests. A 150 W commercial tungsten halogen lamp was vertically placed outside and above the reactor and the lamp was turned on when adsorption–desorption equilibrium was achieved. Reactor outlet connected to the NO_x analyzer (Thermo Scientific, 42i-TL). Opening light source after NO concentration being stable and every 1 min sampling inspection and record via NO_x analyzer. The removal ratio (η) of NO was calculated as $\eta = (1\text{-}C/C_0) \times 100\%$, where C and C_0 are the concentrations of NO in the outlet steam and the feeding stream, respectively.

3. Results and discussion

3.1. Materials and structures

C N-O La was successfully synthesized via the facile co-pyrolysis of the mixture of urea and $La_2(CO_3)_3$. Representative XRD patterns (Fig. 1a) reflect that the pristine CN has two characteristic diffraction peaks at around 13.1° and 27.2° as reported previously. The former one arises from the in-plane structural packing motifs, namely, the lattice planes parallel to the c-axis. The later one is attributed to the long-range interplanar stacking of aromatic systems [33–35]. Obviously, the two sharp peaks disappear gradually with the increased usage of $La_2(CO_3)_3$ as depicted by the arrows in C N-O La patterns (Fig. 1a). Furthermore, the two characteristic peaks of C N-O La-50 vanish completely in comparison with pristine CN, which indicates the formation of amorphous carbon nitride with unique atomic arrangement of short-range order but long-range disorder. The amorphization of CN could be further certified via the FT-IR spectra (Fig. 1b) and demonstrated by DFT method (Fig. 2a and b).

The FT-IR spectra (Fig. 1b) reveal that the original graphitic C–N network shows almost no change after the introduction of $La_2(CO_3)_3$. The characteristics of the condensed C–N heterocycles [36–39], for instance, the typical breathing mode of the tri-s-triazine units at 810 cm^{-1} and remain unchanged. The stretching mode of C–N heterocycles in the 1200–1650 cm^{-1} region witnesses on variation in band position of C N-O La, but are found to be weakened and even disappeared with high dosage of $La_2(CO_3)_3$. This observation can be

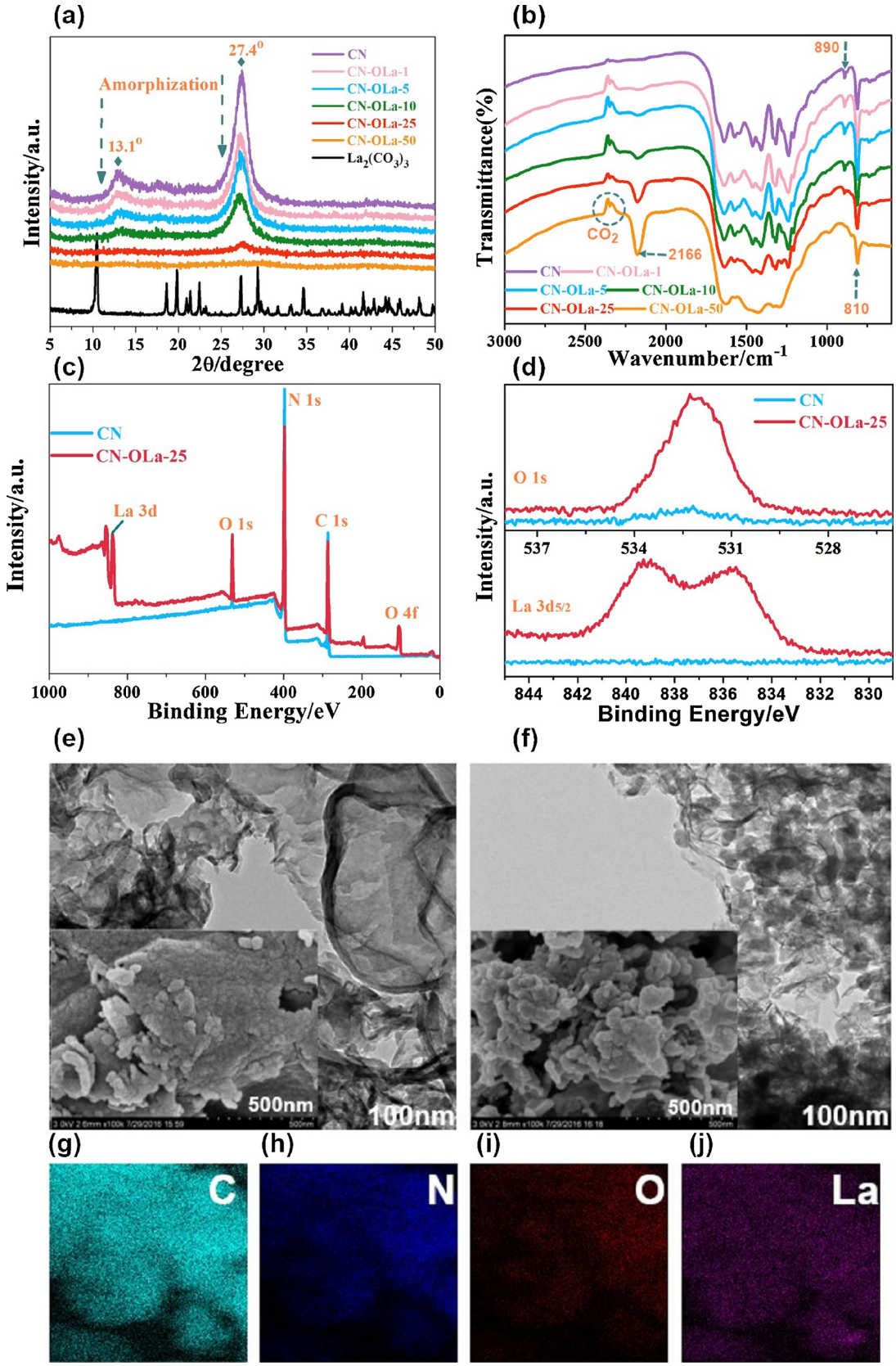

Fig. 1. XRD patterns (a); FT-IR spectra (b); XPS full survey spectra (c); XPS spectra of O 1s and La 3d (d); Typical TEM and SEM (inset) images of CN (e) and C N-O La (f); FESEM-EDX elemental mapping of C N-O La (g–j).

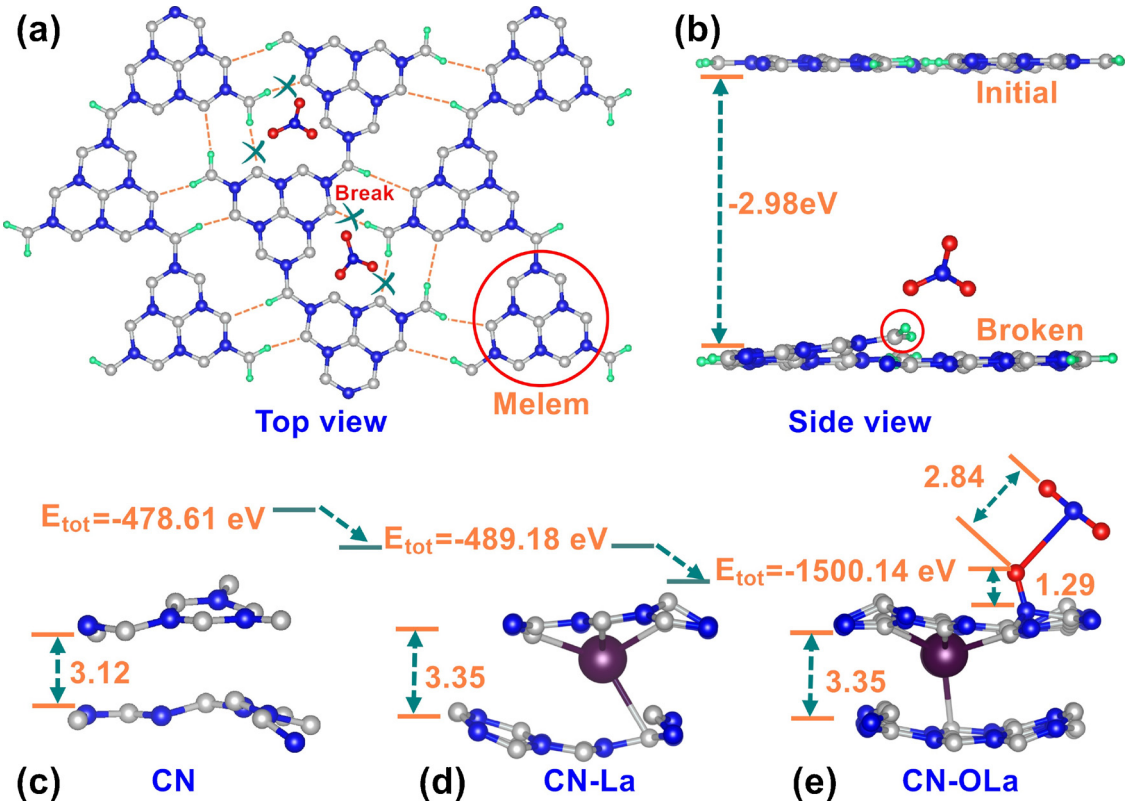

Fig. 2. Schematic illustration of the formation mechanism of amorphous graphitic carbon nitride (a, b); the optimized local structures of individual CN (c), La-doped CN (d), O-La-doped CN (e). All lengths are given in Å, and blue, gray, green, red and purple spheres depict C, N, H, O and La atoms, respectively.

Table 1
The maximum and equilibrium NO removal ratios (η_{max} and η_{equ}), specific surface areas (S_{BET}) and pore volumes for individual CN, and C N-O La samples.

Sample	η_{max},%	η_{equ},%	S_{BET},m^2/g	Pore volume cm^3/g
CN	39.62	35.80	65	0.37
C N-O La-1	44.26	43.65	70	0.37
C N-O La-5	47.66	47.66	68	0.35
C N-O La-10	48.48	47.66	86	0.47
C N-O La-25	51.90	50.40	78	0.38
C N-O La-50	34.98	28.57	43	0.14

attributed to the unique effect of CO_3^{2-} that could destroy the hydrogen bond and the CO_2 is released in the process of amorphization under high temperature treatment. Thus, the corresponding peak at 890 cm^{-1} assigned to the deformation mode of N—H is gradually diminished and the increased peaks at 2300–2400 cm^{-1} (assigned to CO_2), are observed on the spectra of C N-O La [40–42]. Moreover, the newly generated peak at 2166 cm^{-1} (assigned to the stretching vibration of N = C=N) can be observed in C N-O La, which indicates that CO_3^{2-} only destroys the periodic interlayers melon arrangement but maintains the basic strands atomic structures to afford unique amorphous arrangements of short-range order and long-range disorder [41].

In addition, the signals of C, N, O and La elements could be revealed in the full survey spectra (Fig. 1c). The La and O elements could also be well identified, with a binding energy located at their corresponding peaks in the XPS patterns (Fig. 1d). This result demonstrates the successful introduction of O and La into CN. The increased content of O in C N-O La-25 should be attributed the decomposition of CO_3^{2-} fromm $La_2(CO_3)_3$. Besides, the typical SEM and TEM images (Fig. 1e and f) illustrate that the continued layers of CN is destroyed into stacked fragment in C N-O La. The HRTEM images in Fig. S3 clearly shows that the lattice of the catalyst cannot be observed, which further demonstrated the formation of amorphous carbon nitride. This result implies that the introduction of CO_3^{2-} can influence the morphology and induce the amorphization of pristine CN. The elemental signals of C, N, O and La can be detected in the mapping images of C N-O La-25 (Fig. 1g–j), verifying the homogenous dispersion of O and La elements across the sample. The slightly increased specific surface areas (S_{BET}) and pore volumes in C N-O La (Table 1) are observed, which indicates that the specific surface areas are not the key factor in the enhanced photocatalytic activity of C N-O La. Note that the sharply lowered S_{BET} and pore volumes in C N-O La-50 (Table 1) are found as well. This can be ascribed to the fact that excessive $La_2(CO_3)_3$ may block the pore structure, leading to low surface areas.

The formation of amorphous carbon nitride also is further examined by ab initio molecular dynamics (AIMD) simulation with adsorbed CO_3^{2-} on CN to test geometric structure variations of monolayer CN at 800 K in vacuum. As shown in Fig. 2a, both the atomic coordination within each melon unit and the C-N -C coordination between two nearest neighboring melon units within each polymeric strand remain unchanged, consistent with the tri-s-triazine units at 810 cm^{-1} of C N-O La observed in FT-IR spectra (Fig. 1b). The breaking of in-plane hydrogen bonds between strands of polymeric melon units by the adsorption of CO_3^{2-} could be depicted in Fig. 2a. In contrast to the initial condition, the interaction between CO_3^{2-} and hydrogen bonds is apparently strengthened. The adsorption energy of CO_3^{2-} on CN is decreased by 2.98 eV under the attack of CO_3^{2-} (Fig. 2b). Because of the spontaneous chemical interaction between CO_3^{2-} and CN, the planar CN becomes tilted. This result suggests that the CN monolayer shows a tendency to get disordered after the adsorption of CO_3^{2-} on CN. As Fig. 2a displayed, the in-plane hydrogen bonds between strands of polymeric melon units are broken and thus the amorphous carbon nitride is formed.

The C–O bond (belong to pristine CO_3^{2-}) length (2.84 Å) is significantly longer than that of the C–O bond (formed after adsorption of

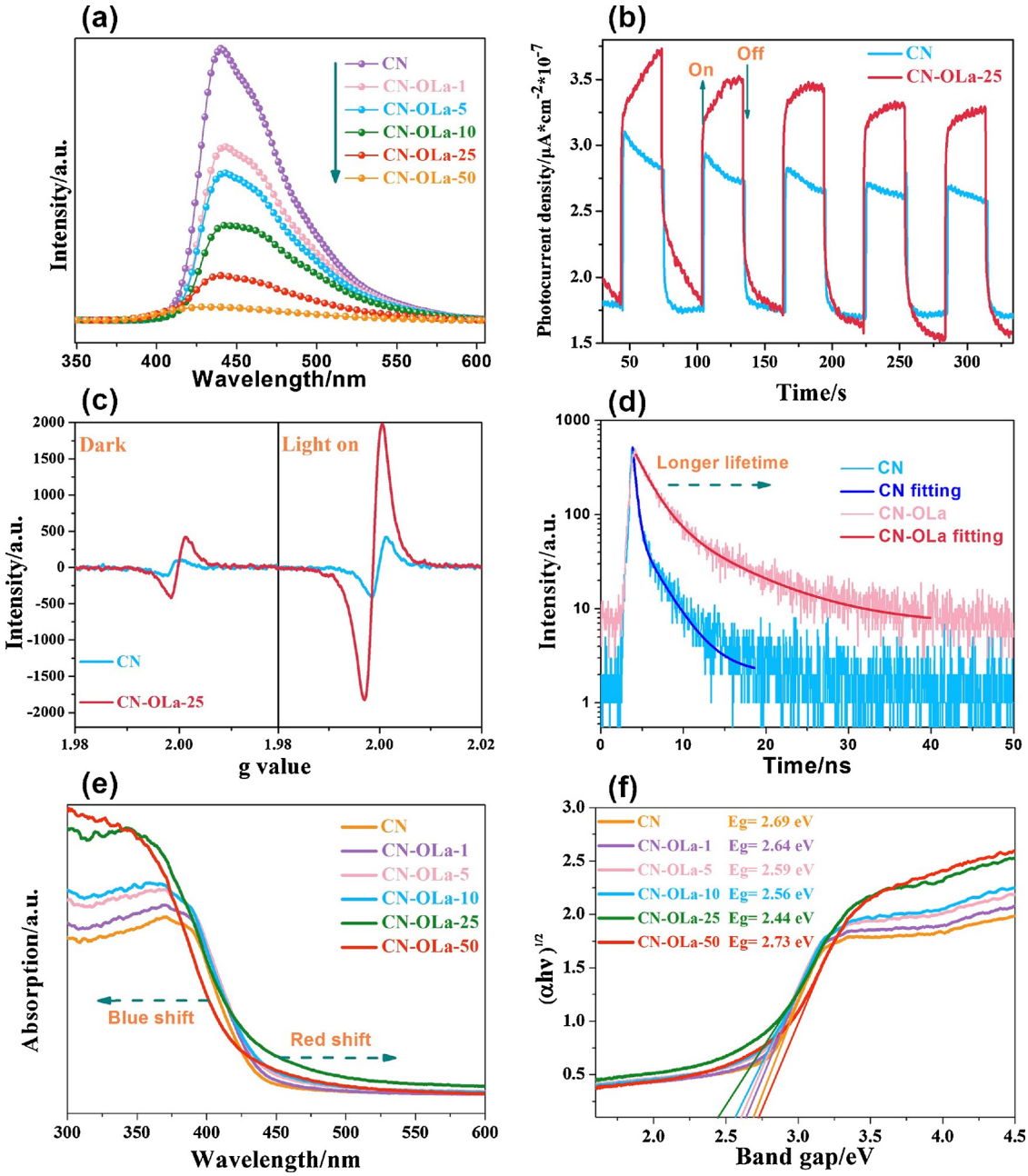

Fig. 3. Photoluminescence spectra of as-obtained samples (a); transient photocurrent responses (b); Low temperature EPR spectra (c); ns-level time-resolved fluorescence spectra surveyed at room temperature (d); UV–vis DRS spectra (e); estimated band gaps (f).

CO_3^{2-} on CN) length (1.29 Å) in Fig. 2e, suggesting that the C–O bond (primordially belong to CO_3^{2-}) is inclined to be broken so that the CO_2 would be released during the co-pyrolysis when the in-plane hydrogen bonds are broken by CO_3^{2-}. This is also consistent with results in FT-IR (Fig. 1b). Moreover, the DFT calculation result indicates that the La atom is stably intercalated between adjacent CN layers. The CO_3^{2-} is adsorbed on the surface of CN layer and is finally decomposed, leaving O atom on CN (Fig. 2c–e). This is supported by the proof of increased heat release: $E_{tot=}$-1500.14 eV (C N-O La) < $E_{tot=}$ −489.18 eV (CN-La) < $E_{tot=}$-478.61 eV in Fig. 2c–e (Detailed information in Fig. S1). Evidently, the interlayer distance of La-intercalated CN (3.35 Å) is enlarged in comparison with the pristine CN (3.12 Å).

Additionally, the X-ray absorption fine structure (XAFS) to further study the coordination environment of La atoms in Fig. S2 and Table S1. The X-ray absorption near-edge structure (XANE) spectra reveals the line intensities of $La(OH)_3$ and C N-O La show similar trend, indicating that La from C N-O La still remained fully oxidized (Fig. S2a). In the Fourier transforms (r space, Fig. S2b) there are two prominent peaks at ~2.0 Å and ~4.0 Å from the La-O and La-La contributions, respectively. Owing to the high disordering in the higher shells, only the two main peaks in the r range of 1.0–4.5 Å were considered in the EXAFS curve-fitting (fitting parameters are given in Table S1). Obviously, the La-O coordination decreases from ca. 9.0 to 4.8, which shows the changed coordination for La atoms over C N-O La. Also, the bond length of La-O is increased from 2.65 to 2.75 Å in C N-O La. Combined with the result of the electronic location function (ELF, Fig. 4b), La atoms were inclined to proceed the coordinate with N atoms, thus, the decreased La-O coordination should be attributed to increased La-N coordination in C N-O La. These results conclusively indicate the successful fabrication of O/La co-functionalized amorphous carbon nitride.

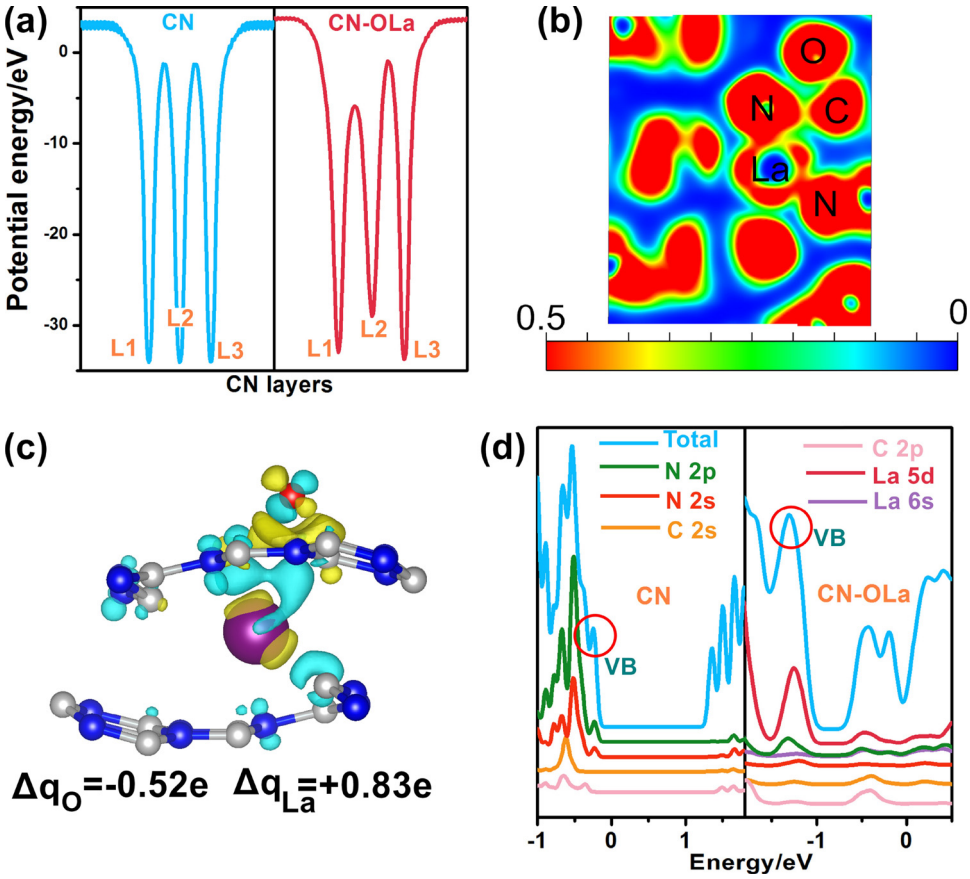

Fig. 4. The electrostatic potential (a); the electronic location function (b); the charge difference distribution between O-La atoms and CN layers (c), charge accumulation is in blue and depletion is in yellow; the projected density of states (PDOS) for C, N and La atoms in CN layers with Fermi level set to 0 eV (d).

3.2. Electron delivery mechanism

Charge mobility is analyzed to better uncover the mechanism of electron delivery. As shown in PL spectra (Fig. 3a), the charge carriers separation are promoted via O/La co-functionalization. The photocurrent response (Fig. 3b) measurement is also carried out to distinguish the variation of photoelectric response after introducing O and La. C N-O La-25 exhibits an enhanced photocurrent under visible-light irradiation, in comparison with CN, indicating more efficient separation of photogenerated electron/hole pairs [43].

Low temperature solid-state EPR spectra (Fig. 3c) are employed to demonstrate the extension of the graphitic π -conjugated system in the CN planes. All samples show a strong Lorentzian line at g value of about 2.0 in the dark, confirming the existence of unpaired electrons on the π-conjugated graphitic hexagon rings [44,45]. In contrast to pure CN, the EPR intensities of C N-O La-25 are stronger and greatly strengthened following the visible-light irradiation for 15 min, which implies that the O/La co-functionalization could enormously boost the electron mobility and accelerate the charge transportation. Further, nanosecond-level time-resolved fluorescence decay spectra are employed to define the electron delivery dynamics in the respective samples (Fig. 5d). The curves can be fitted well to a biexponential decay function. All the fitting parameters are summarized in Table 2. Significantly, the short lifetime (τ_1) and the long lifetime (τ_2) of the charge carriers are evidently prolonged after O and La incorporation comparing to pristine CN. The prolonged lifetime of charge carriers can increase their probability to participate in photocatalytic reactions before recombination [43]. These results together confirm that the O/La co-functionalization and amorphization of CN could highly promote the charge carriers separation and transfer. The specific role of O/La co-functionalization on charge delivery will be further studied via DFT (Fig. 4a–d).

The light adsorption properties of these samples are measured. In comparison with pristine CN, the C N-O La samples (except C N-O La-50) exhibit red shifts of absorption edge (Fig. 3e), thus extending the visible light absorption [12]. The corresponding band gaps are determined from the intercept of tangents to the plot of $(\alpha h\nu)^{1/2}$ *vs.* photoenergy (Fig. 3f). The gap energy (E_g) is in the order of C N-O La-50 (2.73 eV) > CN (2.69 eV) > C N-O La-1 (2.64 eV) > C N-O La-5 (2.59 eV) > C N-O La-10 (2.56 eV) > C N-O La-25 (2.44 eV). The increased light absorption and decreased band gaps of C N-O La samples except C N-O La-50. The reduced band gap of catalysts can be ascribed to the La-doping. The enlargement of the band gap can be attributed to the amorphization of CN [12]. In contrast to other C N-O La samples, C N-O La-50 exhibited decreased light absorption (blue shift could be observed in Fig. 3e) and increased band gap in Fig. 3f. This should be ascribed to high dosage of $La_2(CO_3)_3$ that could thoroughly break the structure of CN. According to above results, the optimized ratio of $La_2(CO_3)_3$/CN is 25%. The C N-O La-25 demonstrates broadened visible light absorption and enhanced charge separation, and thus potentially exhibiting highly enhanced NO removal efficiency (Fig. 5a).

Moreover, we analyzed the effect of O/La co-functionalization on the electron delivery of carbon nitride via DFT calculation. Fig. 4a depicts the electrostatic potentials of CN and C N-O La. Therein, the valley bottom denotes the position of the CN layer, and the highest peak position signifies the lowest energy barriers that electrons need to stride over the layers. As shown in Fig. 4a, a high potential barrier of about -32.83 eV prohibits the charge carriers transportation between the adjacent layers (CN) for the pristine g-C_3N_4. Interestingly, the electrostatic potential between the first layer (L1) and second layer (L2) is elevated from -32.83 eV to -23.43 eV for C N-O La. Such decreased energy barriers enables electron transfer toward the Z direction, which makes the construction of the interlayer electron delivery channels (L2 → La →

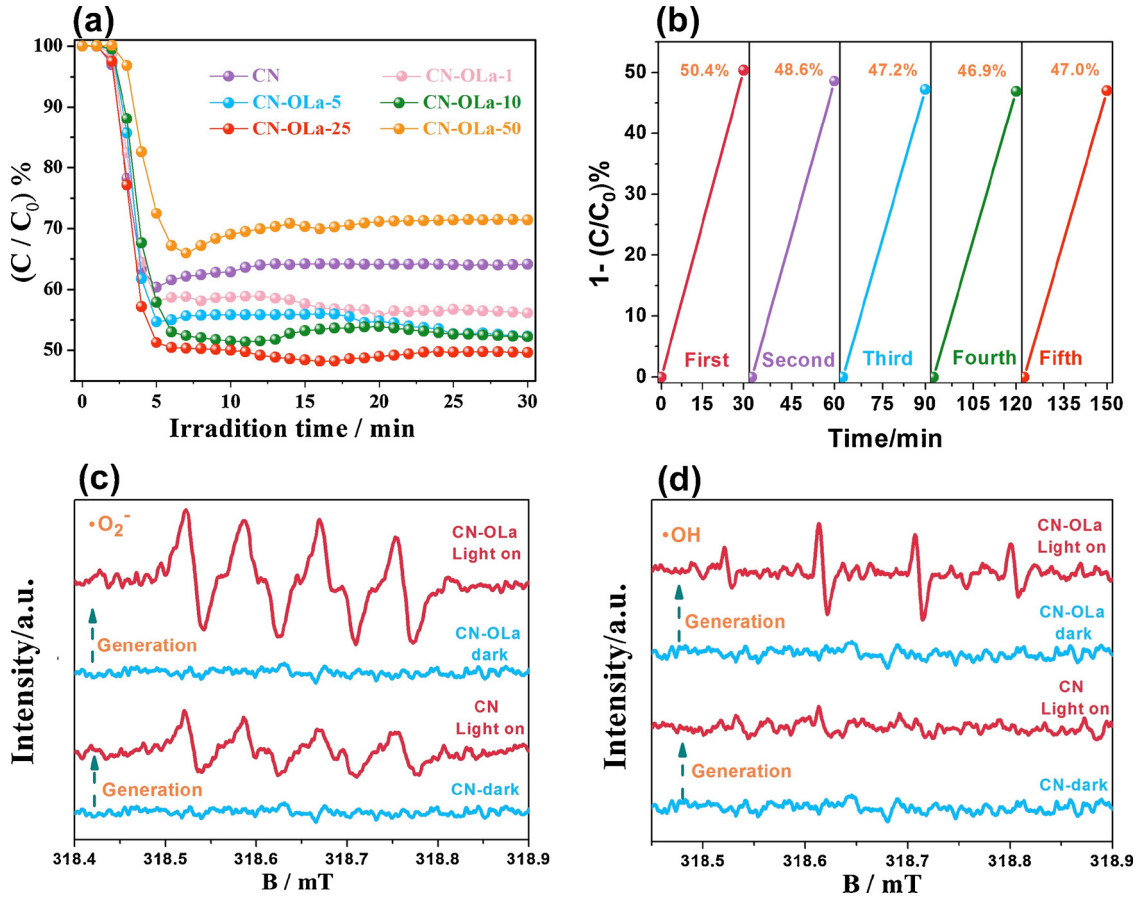

Fig. 5. Photocatalytic activity in NO removal (a); cycling tests for C N-O La-25 (b); DMPO ESR spectra in the dark and under visible-light for 15 min, respectively, in a methanol dispersion for O_2^- (c) and an aqueous dispersion for OH (d).

Table 2
Kinetic Parameters of the Fitting Decay Parameters of CN and C N-O La-25.

Samples	Parameters	Life time (ns)	Relative percentage (%)	χ^2
CN	τ_1	0.39	51.89	1.055
	τ_2	2.74	48.11	
C N-O La-25	τ_1	2.03	46.86	1.129
	τ_2	8.23	53.14	

L1→ O) feasible.

Besides, the electronic location function (ELF, Fig. 4b) indicates that there exists strong electron localization via O/La co-functionalization, which could provide an efficient electronic channel for interlayer electron transfer in C N-O La. The charge difference distribution (Fig. 4c) displays that the covalence exists between La and L1. The total charges (Δq) value of La and O atoms, calculated using the Bader method [46], are +0.83 and -0.52 e, respectively. The positive value of Δq means that the electrons of La atoms are donated mainly to the N atoms in L1, based on the primary region of the charge difference distribution. Then the negative value of Δq of O atoms indicates the electrons are transferred to O atoms owing to its strong electronegativity, and thus the activated oxygen species (typically, O_2^-) are formed. These results are consistent with the interlayer electron delivery channels (L2 → La → L1→ O) presented above. Besides, the ability of donating electrons by La atoms at valence-band (VB) maximum as confirmed in Fig. 4d. The La atoms donate the 5d electrons and then ionically combined with in-planar N atoms, corresponding to the charge difference distribution and electron location function analysis.

The electron transportation channels (L2 → La → L1→ O), by sandwiching O and La atoms between CN layers, could critically reduce the energy barriers for electron transfer between adjacent layers and finally induce the charge carriers to the surface of CN. This could effectively prohibit the recombination of carriers and boost the separation and transportation efficiency of charge carriers. Consequently, O_2 molecules could directly be activated to form abundant reactive species for photocatalytic redox reactions via these localized electrons through the electrons transfer process (L2 → La → L1→ O).

3.3. Photocatalytic activity and stability

The photocatalytic performances of the pristine CN and C N-O La samples have been measured for NO removal under visible-light irradiation (Fig. 5a). All the C N-O La samples except C N-O La-50 exhibit enhanced photocatalytic activity, superior to that of original CN, indicating that O/La co-functionalization is an effective strategy for advancing the photocatalysis efficiency of CN. However, compared to pristine CN, C N-O La-50 displayed terrible photocatalytic performance because of the lower S_{BET} and destroyed structure of C N-O La-50. Importantly, the C N-O La-25 maintains an optimal photocatalytic activity for 30 min with an equilibrium removal NO ratio of 50.4%. The removal ratio undergoes a very slight reduction from 50.4 to 47.0% after repeated runs (Fig. 5b), which implies that C N-O La-25 is an efficient and stable photocatalyst. The optimized maximum NO removal efficiency could surpass the reported Na/K-doped CN (roughly 22.0%～44%), $Bi_2O_2CO_3$/g-C_3N_4 (34.8%), I-doped $BiOIO_3$ (44.1%), and Ag-TiO_{2-x} (45.0%) under visible light irradiation. Thus, it can be concluded that the C N-O La-25 is indeed an excellent photocatalyst for NO removal [20,47–49].

The reactive species responsible for photocatalytic NO removal and the reason for enhanced photocatalytic activity have been further

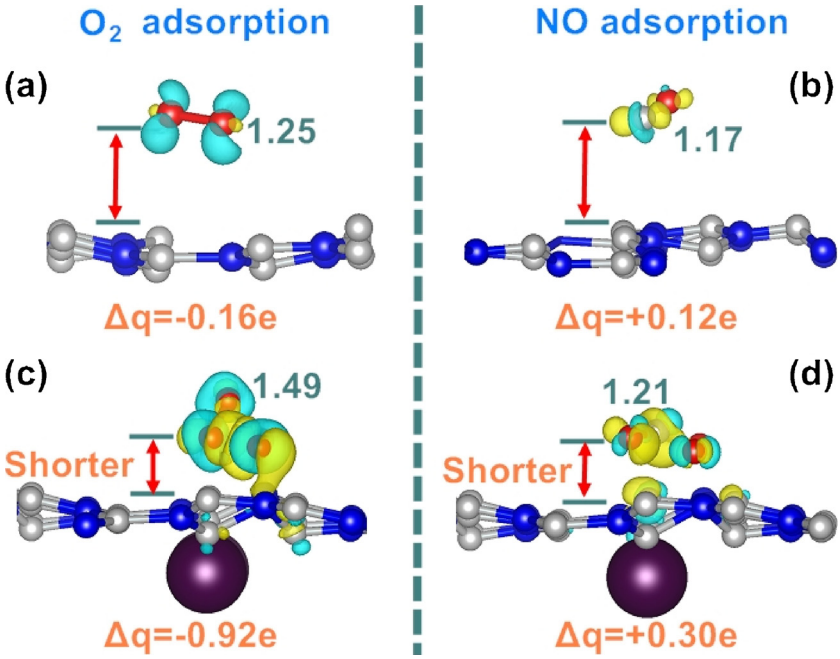

Fig. 6. Optimized O_2 adsorption in CN (a) and C N-O La (c); optimized NO adsorption in CN (b) and C N-O La (d). Δq stands for total charge for O_2 and NO molecules. Negative and positive values for Δq depict electron accumulation and depletion, respectively. All bond lengths are given in Å.

investigated by DMPO spin-trapping ESR. As expected, stronger DMPO-O_2- signals can be observed for C N-O La-25 than for CN (Fig. 5c). The improvement is directly associated with the enhanced molecular oxygen activation by localized electrons and subsequently generating more superoxide radicals (O_2-) for photocatalysis reaction. Meanwhile, the OH radicals in C N-O La-25 can be detected (Fig. 5d), which is formed via the route $O_2^- \rightarrow H_2O_2 \rightarrow$OH.

Further, the mechanism for electron localization enhanced activation of O_2 and NO molecule via O/La co-functionalization is verified by DFT calculations. As shown in Fig. 6a–d, we first optimize the geometric structure of O_2 and NO adsorption on CN. Intriguingly, the distances of O_2 and NO adsorption over C N-O La become shorter than that over the pristine CN. These results demonstrate that the introduction of O and La could facilitate O_2 and NO adsorption and activation. Indeed, the O—O bond length in C N-O La is activated to be 1.49 Å, longer than that (1.25 Å) in pure CN. Analogously, the N–O bond length in C N-O La is elongated from 1.17 of CN to 1.21 Å. Those results suggest that the electron localization by O/La co-functionalization could tremendously weaken the O—O and N–O bonds and thus enhance the molecular O_2 and NO activation on catalyst surface.

Furthermore, the charge difference distribution (Fig. 6c–d) is provided to intuitively illustrate the gain or loss of electrons between the O_2 (or NO) during molecular activation. In contrast to pristine CN, the electrons transfer between O_2 (or NO) and surface O atom of C N-O La is apparently enhanced, which can be attributed to the strong electronegativity of O atom. In fact, the total charge (Δq) of O_2 (or NO), calculated by the Bader method, is increased from -0.16e to -0.92e (NO, from +0.12e to +0.30e) on O/La co-functionalized carbon nitride. The molecular O_2 obtain the localized electrons from O atom and would be activated to O_2^- and OH radicals, in correspondence with the DMPO-O_2- and DMPO-OH results (Fig. 5c–d). Additionally, the molecular NO lost electrons to O atom and would be activated to NO^+, corresponding to the broad bonds at 2300-2200 cm^{-1} assigned to NO^+ appeared in the *in situ* FT-IR spectra of C N-O La (later discussed in Fig. 7e–f). These results reveal the mechanism of improved photocatalytic performance of C N-O La via electron localization: (1) the enhanced O_2 activation through localized electrons could facilitate the production of O_2^- and OH to participate in the photocatalytic redox reaction, and the enhanced NO adsorption capacity on C N-O La could motivate the formation of oxynitride intermediates (e.g. NO^+) and thus accelerate NO convert to final products.

3.4. *In situ DRIFTS investigation and photocatalysis reaction mechanism*

in situ DRIFTS studies are further performed to understand how such electronic optimization influences NO adsorption and photocatalytic NO oxidation processes. Fig. 7a–b and e–f reveal the time-dependent evolution of the FT-IR spectra during the NO adsorption process and photocatalytic NO oxidation process over pristine CN, respectively. Distinctly, there are some identical bands existed for both NO adsorption and oxidation processes. But certain new bands (e.g. at 965 cm^{-1}, 1060 ~ 1003 cm^{-1} and 2121 cm^{-1}) could be observed in NO oxidation process. Table S2 summarizes the possible assignments of the observed bands. The bands at 1843, 1172, 1160 and 1142 cm^{-1} could be attributed to NO-/NOH [42,50,51], and the band at 1787 cm^{-1} might be assigned to physically absorbed NO [52]. Those results indicate the disproportionation of NO adsorbed on surface of CN, which may be derived from the following reaction: 3NO + OH- = NO_2 + NO- + NOH [53,54]. Although NO_2 was not detected probably because of its short lifetime and immediately transformed to other nitrate species (e.g. NO_3-). This fact is well certified by the appearance of the bands at 1109 and 1001 cm^{-1}, assigning to bidentate and bridging nitrates (NO_3-) [42,55,56], following the reaction bellow: NO- + 2NO_2 → NO_3- + 2NO [50]. Additionally, the weak band at 965 cm^{-1}, assigned to N_2O_3 [22,57], could be found during photocatalytic NO oxidation, which may be due to the chemical reaction between NO and activated radical (OH): 2NO + 2OH → N_2O_3 + H_2O. Additionally, the new band at 2121 cm^{-1} assigned to NO_2^+ [54], could be observed over pristine CN under light irradiation in Fig. 7e, following reaction: NO_2 + OH → NO_2^+ + OH-. Furthermore, other adsorption bands are developed progressively and can be attributed to the stretching of bidentate (at 1109 and 1060 ~ 1003 cm^{-1}), bridging (at 1001 cm^{-1}) nitrates, chelating bidentate (at 986 cm^{-1}) nitrates, NO_2- (at 885 cm^{-1}) and chelating nitrites (869 cm^{-1}) [22,52,54–56]. The formation of nitrites and nitrates in NO adsorption process on CN might be ascribed to the active pyridine nitrogen sites embedded inside the carbon matrix, which could facilitate the formation of activated oxygen species and then enhanced the NO oxidation capacity of surface oxygen species. The newly formed nitrates (1060 ~ 1003 cm^{-1}) over CN during photocatalytic NO oxidation process can be attributed to the increased surface oxygen species

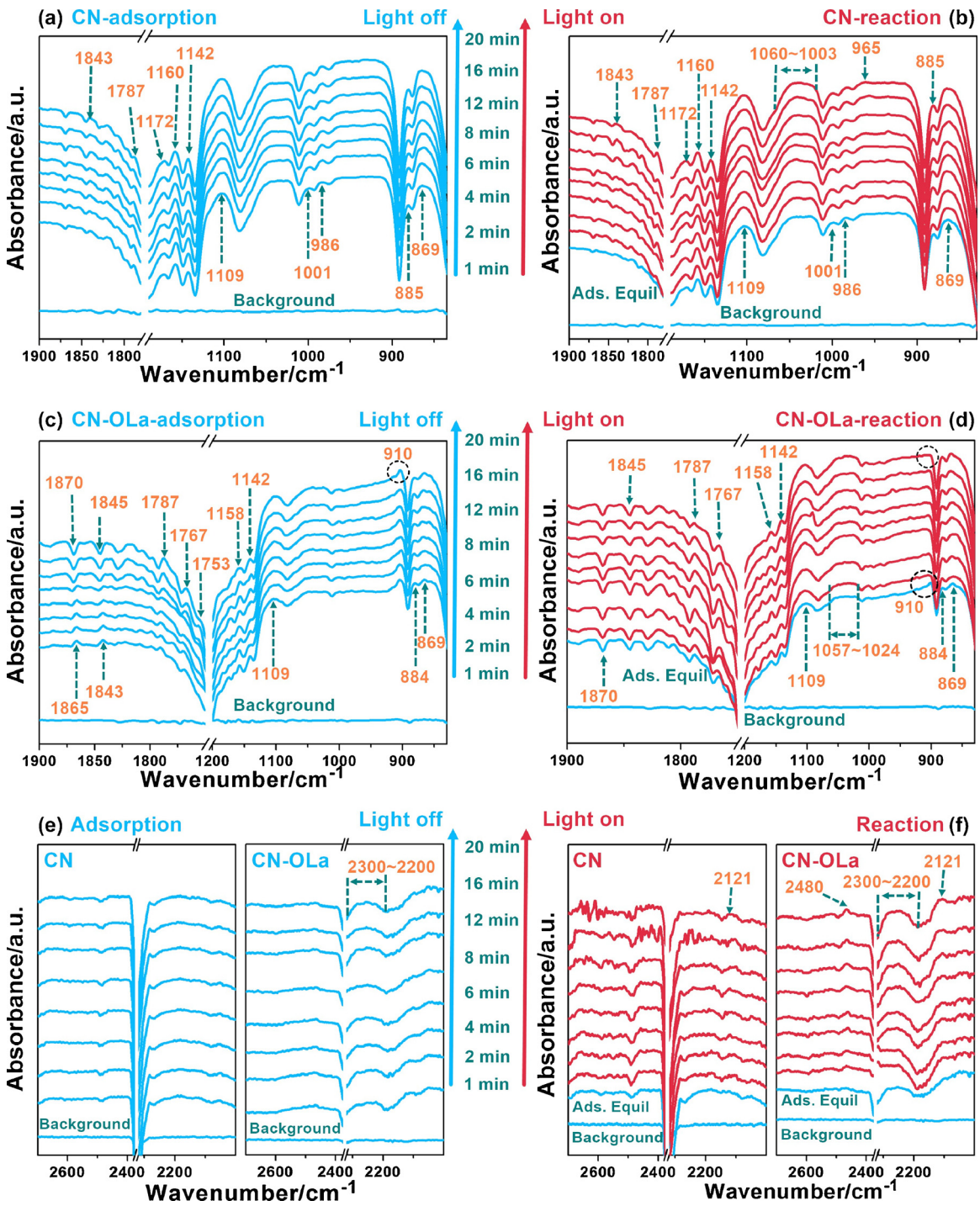

Fig. 7. *in situ* FT-IR spectra of NO adsorption and visible light reaction processes over CN and C N-O La.

(O_2-) derived from the photo-generated electrons captured by the adsorbed O_2. The O_2– radicals with high oxidation capability could transform the intermediates (NO-/NOH, N_2O_3) to final products (nitrates). The final products could be removed easily by water washing and the photocatalyst can be regenerated via this facile method.

In the case of C N-O La, the absorption product of nitro hybrids can be observed before the visible-light irradiation as shown in Fig. 7c and e. Table S3 summarizes the possible assignments of the observed bands. In contrast to NO adsorption over CN, some similar NO adsorbed bands could be found as well in the NO adsorption over CN–OLa. However, the crucial differences between two cases can be identified. The bands at 1865 and 1843 cm^{-1}, assigned to NO and NO-/NOH [50], respectively, are developed progressively during 1 ~ 8 min of NO adsorption. But they are suddenly disappeared and replaced by the appearance of the bands at 1870 and 1845 cm^{-1}, assigned to NO [50,52], which are developed after 8 min of NO adsorption. Synchronously, the intensities of the bands at 1878 and 1867cm^{-1}, both assigned to NO, are dramatically increased after 8 min of NO adsorption. Certainly, the unchanged bands at 1158 and 1142 cm^{-1} attributed to NO-/NOH [42,50], could be obviously observed during whole NO adsorption. Those results indicate the NO adsorption and intermediates formation processes, corresponding to the following reaction: 3NO + OH- = NO_2 + NO- + NOH. Moreover, the bands of nitrates (at 1109, 1001 and 986 cm^{-1}) and nitrites (at 884 and 869 cm^{-1}) could be found as well

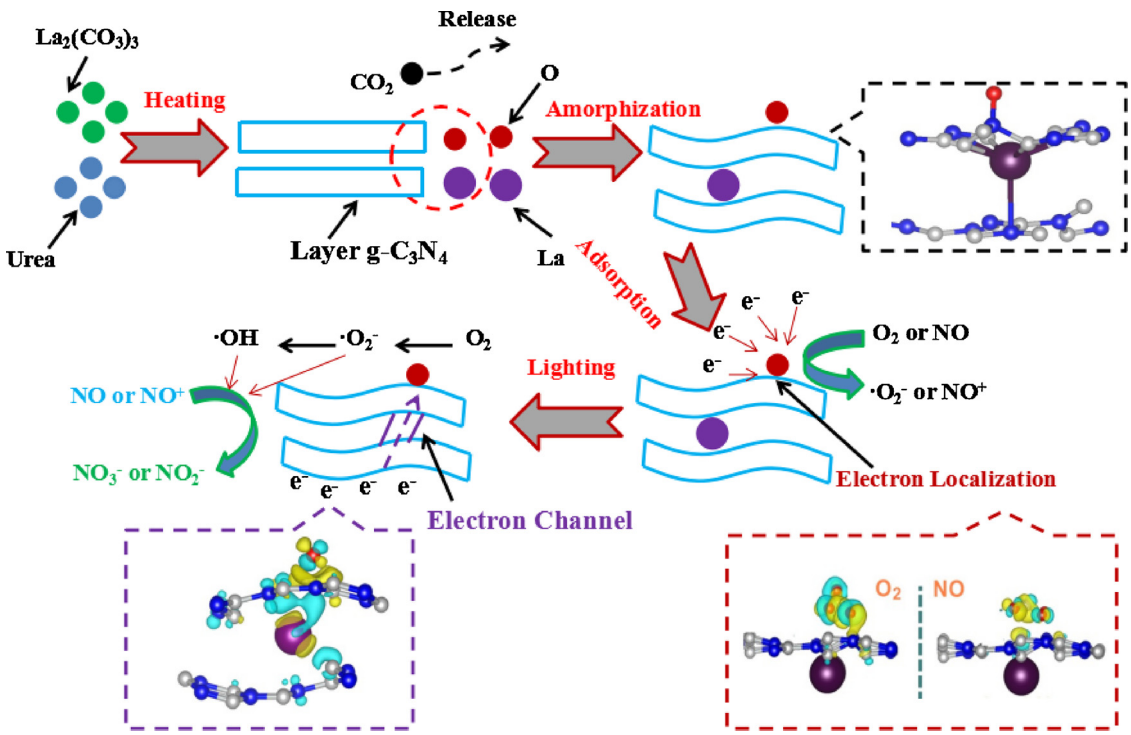

Fig. 8. The illustrations of the catalyst design and the effect of O/La co-functionalization on the charge separation, reactants activation and photocatalysis mechanism.

[22,42,50]. The NO_2 is not detected as well over C N-O La during NO adsorption, similar to that of pristine CN. Notably, the broad bonds at 2300 ~ 2200 cm^{-1}, assigned to NO^+ [50,58], could be obviously observed over C N-O La in Fig. 7e, which can be attributed to electron exchange between NO and O atom via the localized electrons on O/La co-functionalized amorphous carbon nitride (Fig. 6d). Additionally, another possible intermediate (N_2O_4) bands at 1753 and 910 cm^{-1} appeared during NO adsorption of C N-O La following reaction: $2NO_2 \rightarrow N_2O_4$ [22,57,58].

In comparison to the NO absorption process, the intensity of bands at 1753 and 910 cm^{-1} is gradually decreased after visible-light irradiation and new broad bands at 1057 ~ 1024 cm^{-1} and 2480 cm^{-1} assigned to nitrates [59,60], appear during photocatalytic NO oxidation process on C N-O La. Those results may reveal the conversion of intermediate (e.g. N_2O_4, NO^+ and NO-/NOH) into final products (nitrates) via superoxide (O_2-) or hydroxyl (OH) radicals. In addition, the new band at 2121 cm^{-1} (assigned to NO_2^+) appeared and the intensity is increased following the reaction: $NO_2 + OH \rightarrow NO_2^+ + OH$-.

3.5. Schematic illustrations of the catalyst design and the effect of O/La co-functionalization on the charge separation, reactants activation and photocatalysis mechanism

As shown in Fig. 8, O/La co-functionalized amorphous carbon nitride (C N-O La) can be fabricated via the co-pyrolysis of urea with the $La_2(CO_3)_3$. The electrons are mainly localized around O atom on the surface of CN owing to its strong electronegativity, which could promote reactants activation (generated NO^+ or O_2^-) and thus enhance the photocatalytic reaction. Simultaneously, the formation of electronic channels for directional electron delivery in the interlayers (L2 → La → L1→ O) could reduce the energy barriers for photogenerated electron transfer between adjacent layers and facilitate the generation of activated species (e.g. O_2- and OH radicals). Then, the NO or NO^+ are finally converted the final products of NO_3^- via the radicals of O_2- or OH.

4. Conclusions

The O/La co-functionalized amorphous carbon nitride was fabricated via the co-pyrolysis of urea with the $La_2(CO_3)_3$. With a highly combined experimental and theoretical approach, we found that the in-plane hydrogen bonds between strands of polymeric melon units would be broken by CO_3^{2-} to motivate the amorphization of pristine CN. The highly boosted photocatalytic performance of CN-OLa are closely related to the following two crucial effects: I) The O/La co-functionalization could generate localized electrons and enhance the reactants activation capacity on C N-O La, specifically, motivating the activation of NO to formed oxynitride intermediates (e.g. NO^+) and dramatically inducing O_2 molecules to generate reactive species (e.g. O_2- and OH radicals). This effect could accelerate the conversion of NO to final products. II) The introduction of O and La would construct interlayer directed electron transportation channels (L2 → La → L1→ O), which could reduce the energy barriers for photogenerated electrons transfer between adjacent layers and thus promote the separation and transportation efficiency of carriers, and thus enhancing the photocatalytic efficiency. The *in situ* FT-IR spectra, in combination with ESR spectra and DFT calculations, revealed the conversion pathway of photocatalytic NO oxidation and the photocatalytic promotion mechanism on C N-O La. This could shed new light on modification and understanding of layered photocatalysts for environmental remediation applications.

Acknowledgements

This work was supported by the National Natural Science Foundation of China (51478070, 21822601 and 21777011), the National Key R&D Plan (2016YFC02047), the Innovative Research Team of Chongqing (CXTDG201602014), and the Key Natural Science Foundation of Chongqing (cstc2017jcyjBX0052). The authors also acknowledge the AM-HPC in Suzhou, China for computational support.

References

[1] J. Di, J.X. Xia, H.M. Li, Z. Liu, Nano Energy 35 (2017) 79–91.
[2] A. Kubacka, M. Fernandez-García, G. Colon, Chem. Rev. 112 (2012) 1555–1614.
[3] X. Qian, K. Fuku, Y. Kuwahara, T. Kamegawa, K. Mori, H. Yamashita, ChemSusChem 7 (2014) 1528–1536.
[4] X. Qian, D. Yue, Z. Tian, M. Ren, Y. Zhu, M. Kan, T.Y. Zhang, Y.X. Zhao, Appl. Catal. B 193 (2016) 16–21.
[5] P. Zhang, T. Wang, X.X. Chang, J.L. Gong, Acc. Chem. Res. 49 (2016) 911–921.
[6] H. Wang, Y. Sun, G. Jiang, Y. Zhang, H. Huang, Z. Wu, S.C. Lee, F. Dong, Environ. Sci. Technol. 52 (2018) 1479–1487.
[7] D.H. Deng, K.S. Novoselov, Q. Fu, N.F. Zheng, Z.Q. Tian, X.H. Bao, Nat. Nanotechnol. 11 (2016) 218–230.
[8] W.J. Ong, L.L. Tan, H.N. Yun, S.T. Yong, S.P. Chai, Chem. Rev. 116 (2016) 7159–7329.
[9] Y.L. Li, P.P. Li, J.S. Wang, Y.L. Yang, W.Q. Yao, Z. Wei, J.S. Wu, X.X. Yan, X.F. Xu, Y.H. Liu, Y.F. Zhu, Appl. Catal. B 225 (2018) 519–529.
[10] S. Cao, Y. Li, B. Zhu, M. Jaroniec, J. Yu, J. Catal. 349 (2017) 208–217.
[11] K. He, J. Xie, Z. Yang, R. Shen, Y. Fang, S. Ma, X. Chen, X. Li, Catal. Sci. Technol. 7 (2017) 1193–1202.
[12] Y. Kang, Y. Yang, L.C. Yin, X. Kang, L. Wang, G. Liu, H.M. Cheng, Adv. Mater. 28 (2016) 6471–6477.
[13] W. Cui, J. Li, Y. Sun, H. Wang, G. Jiang, S.C. Lee, F. Dong, Appl. Catal. B 237 (2018) 938–946.
[14] Y.Y. Wang, W.J. Yang, X.J. Chen, J. Wang, Y.F. Zhu, Appl. Catal. B 220 (2018) 337–347.
[15] Z.Y. Wang, Y. Huang, W.K. Ho, J.J. Cao, Z.X. Shen, S.C. Lee, Appl. Catal. B 199 (2016) 123–133.
[16] H.G. Yu, W.Y. Chen, X.F. Wang, Y. Xu, J.G. Yu, Appl. Catal. B 187 (2016) 163–170.
[17] H.J. Yu, S. Rui, Y.X. Zhao, B. Tong, Y.F. Zhao, C. Zhou, G.I.N. Waterhouse, L.Z. Wu, C.H. Tung, T.R. Zhang, Adv. Mater. 29 (2017) 1605148.
[18] W.L. Yang, L. Zhang, J.F. Xie, X.D. Zhang, Q.H. Liu, T. Yao, S.Q. Wei, Q. Zhang, Y. Xie, Angew. Chem. Int. Ed. 55 (2016) 6716.
[19] X.X. Chang, T. Wang, J.L. Gong, Energy Environ. Sci. 9 (2016) 2177–2196.
[20] T. Xiong, W.L. Cen, Y. Zhang, F. Dong, ACS Catal. 6 (2016) 2462–2472.
[21] J.Y. Li, W. Cui, Y.J. Sun, Y.H. Chu, W.L. Cen, F. Dong, J. Mater. Chem. A 5 (2017) 9358–9364.
[22] W. Cui, L.Y. Li, W.L. Cen, Y.J. Sun, S.C. Lee, F. Dong, J. Catal. 352 (2017) 351–360.
[23] J.C. Bünzli, Chem. Rev. 110 (2010) 2729–2755.
[24] J. Shen, L.D. Sun, C.H. Yan, Dalton Trans. 42 (2008) 5687–5697.
[25] F. Wang, X. Liu, Chem. Soc. Rev. 38 (2009) 976–989.
[26] T.P. Ying, Y.Q. Gu, X. Chen, X.B. Wang, S.F. Jin, L.L. Zhao, W. Zhang, X.L. Chen, Sci. Adv. 2 (2016) e1501283.
[27] G. Kresse, J. Furthmüller, Phys. Rev. B 54 (1996) 11169–11186.
[28] J. Furthmuller, J. Hafner, G. Kresse, Phys. Rev. B 53 (1996) 7334.
[29] J.P. Perdew, K. Burke, M. Ernzerhof, Phys. Rev. Lett. 77 (1996) 3865–3868.
[30] P.E. Blochl, Phys. Rev. B 50 (1994) 17953.
[31] G. Kresse, D. Joubert, Phys. Rev. B 59 (1999) 1758.
[32] D.R. Lide, CRC Press (2003).
[33] P. Niu, L.L. Zhang, G. Liu, H.M. Cheng, Adv. Funct. Mater. 22 (2012) 4763–4770.
[34] F. Fina, S.K. Callear, G.M. Carins, J.T.S. Irvine, Chem. Mater. 27 (2015) 2612–2618.
[35] G. Zhang, J. Zhang, M. Zhang, X. Wang, J. Mater. Chem. 22 (2012) 8083–8091.
[36] B.V. Lotsch, M. Doblinger, J. Sehnert, L. Seyfarth, J. Senker, O. Oeckler, W. Schnick, Chem. Eur. J. 13 (2007) 4969–4980.
[37] G.Z. Liao, S. Chen, X. Quan, H.T. Yu, H.M. Zhao, J. Mater. Chem. 22 (2012) 2721–2726.
[38] F. Dong, M.Y. Ou, Y.K. Jiang, S. Guo, Z.B. Wu, Ind. Eng. Chem. Res. 53 (2014) 2318–2330.
[39] Y.J. Cui, Z.X. Ding, P. Liu, M. Antonietti, X.Z. Fu, X.C. Wang, Phys. Chem. Chem. Phys. 14 (2012) 1455–1462.
[40] Z.H. Cheng, A. Yasukawa, K. Kandori, T. Ishikawa, Langmuir 14 (1998) 6681–6686.
[41] R.W. Stevens, R.V. Siriwardane, J. Logan, Energy Fuels 22 (2008) 3070–3079.
[42] W. Cui, J.Y. Li, F. Dong, Y.J. Sun, G.M. Jiang, W.L. Cen, S.C. Lee, Z.B. Wu, Environ. Sci. Technol. 51 (2017) 10682–10690.
[43] Y. Zhou, X.J. Zhang, Q. Zhang, F. Dong, F. Wang, Z. Xiong, J. Mater. Chem. A 2 (2014) 16623–16631.
[44] Z.A. Lan, G. Zhang, X. Wang, Appl. Catal. B 192 (2016) 116–125.
[45] G. Zhang, X. Wang, J. Catal. 307 (2013) 246–253.
[46] R. Bader, Oxford University Press, (1994).
[47] Y. Sun, T. Xiong, F. Dong, H. Huang, W. Cen, Chem. Commun. 52 (2016) 8243–8246.
[48] Z. Wang, Y. Huang, W. Ho, Appl. Catal. B 199 (2016) 123–133.
[49] Y. Duan, M. Zhang, L. Wang, Appl. Catal. B 204 (2017) 67–77.
[50] M. Kantcheva, J. Catal. 204 (2001) 479–494.
[51] K. Hadjiivanov, H. Knozinger, Phys. Chem. Chem. Phys. 2 (2000) 2803–2806.
[52] M. Kantcheva, A.S. Vakkasoglu, J. Catal. 223 (2004) 352–363.
[53] M.Y. Zhang, C.T. Li, L. Qu, M.F. Fu, G.M. Zeng, C.Z. Fan, J.F. Ma, F.M. Zhan, Appl. Surf. Sci. 300 (2014) 58–65.
[54] J.C.S. Wu, Y.T. Cheng, J. Catal. 237 (2006) 393–404.
[55] Y. Zhou, Z.Y. Zhao, F. Wang, K. Cao, D.E. Doronkin, F. Dong, J.D. Grunwaldt, J. Hazard. Mater. 307 (2016) 63–172.
[56] K. Hadjiivanov, V. Avreyska, A. Dimitar Klissurski, T. Marinova, Langmuir 18 (2002) 1619–1625.
[57] L. Jaan, J.R. Ohlsen, Prog. Inorg. Chem. 27 (2007) 465–513.
[58] B. Azambre, L. Zenboury, A. Koch, J.V. Weber, J. Phys. Chem. C 113 (2009) 13287–13299.
[59] W. He, Y. Sun, G. Jiang, Y. Li, X. Zhang, Y. Zhang, Y. Zhou, F. Dong, Appl. Catal. B-Environ. 239 (2018) 619–627.
[60] J. Li, Z. Zhang, W. Cui, H. Wang, W. Cen, G. Johnson, G. Jiang, S. Zhang, F. Dong, ACS Catal. 8 (2018) 8376–8385.